The Different Dynamic Influences of Typhoon Kalmaegi on two Pre-existing Anticyclonic Ocean Eddies

Yihao He[1], Xiayan Lin [1,2,*], Guoqing Han [1],Yu Liu [1,3] and Han Zhang [2,3,*]

1 Marine Science and Technology College, Zhejiang Ocean University, Zhoushan 316022, China;

2 State Key Laboratory of Satellite Ocean Environment Dynamics, Second Institute of Oceanography,

Ministry of Natural Resources, Hangzhou 310012, China;

3 Southern Marine Science and Engineering Guangdong Laboratory (Zhuhai), Zhuhai 519082, China

Correspondence: Xiayan Lin (linxiayan@zjou.edu.cn) and Han Zhang (zhanghan@sio.org.cn)

Abstract: Using multi-source observational data and GLORYS12V1 reanalysis data, we conduct a comparative analysis of different responses of two warm eddies, AE1 and AE2 in the northern South China Sea to Typhoon Kalmaegi during September 2014. The findings of our research are as follows: (1) For horizontal distribution, the area and the sea surface temperature (SST) of AE1 and AE2 decrease by about 31% (36%) and 0.4 ℃ (0.6 ℃).The amplitude, Rossby number (R_o=relative vorticity/Coriolis parameter) and eddy kinetic energy (EKE) of AE1 increases by 1.3 cm (5.7%), $1.4×10^{-2}$ (20.6%) and 107.2 $cm^2.s^{-2}$ (49.2%) after the typhoon, respectively, while AE2 weaken and the amplitude, Rossby number and EKE decreased by 3.1 cm (14.6%), $1.6×10^{-2}$ (26.2%) and 38.5 $cm^2.s^{-2}$ (20.2%), respectively. (2) In vertical direction, AE1 demonstrates enhanced convergence, leading to an increase in temperature and a decrease in salinity above 150 m. The response below the mixing layer depth (MLD) is particularly prominent (1.3 ℃). In contrast, AE2 experiences cooling and a decrease in salinity above the MLD. Below the MLD, it exhibits a subsurface temperature drop and salinity increase due to the upwelling of cold water induced by the suction effect of the typhoon. (3) The disparity in the responses of the two warm eddies can be attributed to their different positions relative to Typhoon Kalmaegi. Warm eddy AE1, with its center locates on the left side of the typhoon's path, experiences a positive work effect as the typhoon passed by. The negative wind stress curl in AE1 triggers a negative Ekman pumping velocity (EPV), further enhances by the converging sinking of the upper warm water, thereby strengthening AE1. On the other hand, warm eddy AE2, situates closer to the center of the typhoon, weakens due to the cold suction caused by the strong positive wind stress curl in the typhoon's center. Same polarity eddies may have different response to typhoons, the distance between eddies and typhoons, eddies intensity and the background field need to be considered.

1. Introduction

Tropical cyclones (TCs), as they traverse the vast ocean, interact with oceanic mesoscale processes, particularly with mesoscale eddies, representing a crucial aspect of air-sea interaction (Shay and Jaimes, 2010; Lu et al., 2016; Song et al., 2018; Ning et al., 2019; Sun et al., 2023). The South China Sea (SCS) experiences an average of six TCs passing through each year (Wang et al., 2007), causing prominent exchange of energy and mass between air and sea interface (Price, 1981). Meanwhile, due to the influence of the Asian monsoon, intrusion of the Kuroshio Current, and complex topography, the Northern South China Sea (NSCS) also encounters frequent eddy activities (Xiu et al., 2010; Chen et al., 2011). These mesoscale oceanic eddies often play significant roles in mass and heat transportation and air-sea interaction. This unique setting offers an exceptional opportunity to investigate the generation, evolution, and termination of mesoscale eddies and their interaction with TCs.

On one hand, from a thermodynamic perspective, TCs derive their development and sustenance energy from the ocean. Pre-existing mesoscale eddies play a crucial role in the feedback mechanism between the ocean and TCs. Cyclonic eddies (cold eddies) enhance the sea surface cooling effect under TCs conditions, resulting in TCs weakening, due to their thermodynamic structures and cold-water entrainment processes that reduce the heat transfer from the sea surface to the TCs through air-sea interaction(Ma et al., 2017; Yu et al., 2021). In contrast, anticyclonic eddies (warm eddies) suppress this cooling effect, leading to TCs intensification (Shay et al., 2000; Walker et al., 2005; Lin et al., 2011; Wang et al., 2018). Warm eddies have a thicker upper mixed layer, which stores more heat. When a TC passes through a warm eddy, it increases sensible heat and water vapor in TC's center, which are closely related to the TC's intensification (Wada and Usui, 2010; Huang et al., 2022). Furthermore, the downwelling within warm eddies hinders the upwelling of cold water, reducing the apparent sea surface cooling caused by the TCs. These processes weaken the oceanic negative feedback effect and help to sustain or even strengthen TC's development. While from a dynamic perspective, TCs cause the strengthening of cyclonic eddies, leading to positive potential vorticity anomalies, then accelerates the currents and exacerbates global warming, ultimately further promotes TCs enhancement (Zhang et al, 2020).

On the other hand, TCs also have a notable impact on the intensity, size, and movement of mesoscale eddies. In general, TCs strengthen cold eddies and can even lead to the formation of new cyclonic eddies

60   in certain situations (Sun et al., 2014), while TCs accelerate the dissipation of anticyclonic eddies (Zhang

61   et al., 2020). The strengthening effect of TCs on cold eddies is related to the positions between cold

62   eddies and TCs, the intensity of eddies, and TC-induced geostrophic response (Lu et al., 2016; Yu et al.,

63   2019; Lu et al., 2023). Cyclonic eddies on the left side of the typhoon track were more intensely affected

64   by the typhoon, and eddies with shorter lifespans or smaller radii are more susceptible to the influence

65   of TCs. The dynamic adjustment process of eddy and the upwelling induced by TC itself leads to changes

66   in the three-dimensional structure of the cyclonic eddies, including ellipse deformation and re-

67   axisymmetrization on the horizontal plane, resulting in eddy intensification. The presence of cold eddies

68   not only exacerbates the sea surface cooling in the post-typhoon cold eddy region but also accompanies

69   a decrease in sea level anomaly (SLA), deepening of the mixed layer, a strong cooling in the subsurface,

70   increased chlorophyll-a concentration within the eddy, and substantial increases in EKE and available

71   potential energy (Shang et al., 2015; Liu and Tang, 2018; Li et al., 2021; Ma et al., 2021).

72   Generally, typhoons lead to a reduction of warm eddies, while the sea surface cooling is not

73   significant, typically within 1℃. However, there is a noticeable cooling and increased salinity in the

74   subsurface layer, accompanied by an upward shift of the 20℃ isotherm, a decrease in heat and kinetic

75   energy (Lin et al., 2005; Liu et al., 2017; Huang and Wang, 2022). Lu et al. (2020) propose that typhoons

76   primarily generate potential vorticity input through the geostrophic response. When a TC passes over an

77   eddy, there is a significant positive wind stress curl within the typhoon's maximum wind radius, which

78   induces upwelling in the mixed layer due to the divergence of the wind-driven flow field. This upward

79   flow compresses the thickness of the isopycnal layers below the mixed layer, resulting in a positive

80   potential vorticity anomaly. By analyzing the time series of ocean kinetic energy, available potential

81   energy (APE), vorticity budget, and potential vorticity (PV) budget, Rudzin and Chen (2022) find that

82   the positive vertical vorticity advection caused the TC to eliminate the warm eddy from bottom to top

83   after passing through. Under the interaction of the strong TC wind stress in the eye area of the TC and

84   the subsurface ocean current field, the early-onset of a near-inertial wake caused the disappearance of

85   the warm eddy. However, the projection of TC wind stress onto the eddy and the relative position of the

86   warm eddy to the TC can lead to different responses. According to the classical description of TC-

87   induced upwelling, strong upwelling occurs within twice the maximum wind radius of the TC center,

88   while weak subsidence exists in the vast area outside the upwelling region (Price, 1981; Jullien et al.,

89   2012). The warm eddy locates directly beneath the TC's path weakens due to the cold suction caused by

90   the TC's center. However, for warm eddies locate beyond twice the maximum wind radius, they are

91   influenced by the typhoon's wind stress curl and the downwelling within the eddy itself, resulting in the

92   convergence of warm water in the upper layers of the eddy, an increase in mixed layer thickness, and an

93   increase in heat content, leading to a warming response to the TC (Jaimes and Shay, 2015).

94   The NSCS encounters high frequency and intense TCs, concurrently, there is notable activity of

95   mesoscale eddies in this region. Based on in-situ datasets, multi-platform satellite measurements, and

96   GLORYS12V1 reanalysis data, we investigate two anticyclonic eddies on upper ocean responses to

97   Typhoon Kalmaegi. This marks the initial effort to characterize the different physical variations induced

98   by TCs within two same polarity eddies, contributing to a better understanding the role played by

99   mesoscale eddies in modulating interactions between TCs and the ocean. Section 2 provides an overview

100   of the data and methods utilized in this research. Section 3 analyzes the physical parameters of warm

101   eddies, vertical temperature and salinity variations, and explores the different responses of warm eddies

102   both inside and outside the typhoon affected region. Section 4 offers a comprehensive discussion and

103   Section 5 gives a summary.

104   **2. Data and Methods**

105   **2.1. Data**

106   The six-hourly best-track typhoon datasets are obtained from the Joint Typhoon Warning Center

107   (JTWC, http://www.usno.navy.mil/JTWC, last access: 3 February, 2021), the Japan Meteorological

108   Agency (JMA,https://www.jma.go.jp/jma/jma-eng/jma-center/rsmc-hp-pub-eg/besttrack.html, last

109   access: 3 February, 2021), and the China Meteorological Administration (CMA,

110   http://tcdata.typhoon.gov.cn, last access: 3 February, 2022). The data contain the TCs' center locations,

111   the minimum central pressure, maximum sustained wind speed, and intensity category. The translation

112   speed of typhoons is calculated by dividing the distance travelled by each typhoon within a 6-hour

113   interval by the corresponding time. In this paper, Typhoon Kalmaegi and tropical storm Fung-wong are

114   studied (Fig. 1).
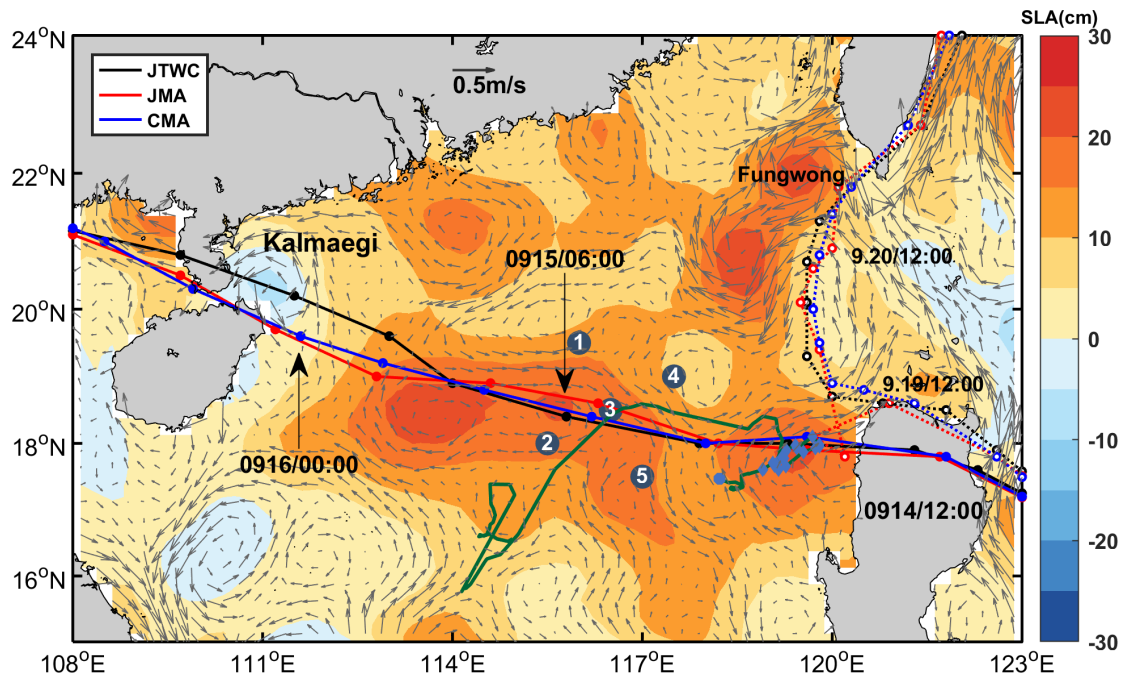
Figure 1. The tracks of Typhoon Kalmaegi (solid lines with dots) and tropical storm Fung-wong (dashed lines with hollow dots) as provide by the Joint Typhoon Warning Center (JTWC, black), Japan Meteorological Agency (JMA, red), and China Meteorological Administration (CMA, blue). The colour shading represents the sea surface level anomaly on 13 September, 2014, while the gray arrows illustrate the geostrophic flow field. The numbered blue dots represent the positions of the five buoy/mooring stations, the green line illustrates the trajectory of Argo 2901469, and the blue diamond's mark the positions of Argo 2901469 inside the eddy AE2 from 26 August 2014 to 25 October 25, 2014.

The daily Sea Level Anomaly (SLA) and geostrophic current data provide by Archiving, Validation, and Interpretation of Satellite Data in Oceanography (AVISO) product (CMEMS, https://marine.copernicus.eu/, last access: 14 Febururay, 2022). This dataset combines satellite data from Jason-3, Sentinel-3A, HY-2A, Saral/AltiKa, Cryosat-2, Jason-2, Jason-1, T/P, ENVISAT, GFO, and ERS1/2. The spatial resolution of the product is 1/4° × 1/4°, the period from 1 September to 30 September 2014 was used.

The daily Sea Surface Temperature (SST) data used in this study is derived from the Advanced Very High-Resolution Radiometer (AVHRR) product data provided by the National Oceanic and Atmospheric Administration (NOAA). The data is obtained from the Physical Oceanography Distributed Active Archive Center (PODAAC) at the NASA Jet Propulsion Laboratory (JPL) (ftp://podaac.jpl.nasa.gov/documents/dataset_docs/avhrr_pathfinder_sst.html, last access: 16 March, 2022). The spatial resolution of the data is 1/4° × 1/4°.

Argo data, including profiles of temperature and salinity from surface to 2000 m depth are obtained from the real-time quality-controlled Argo data base (Euro-Argo, https://dataselection.euro-argo.eu/, last access: 4 April, 2022). We select Argo float number 2901469, situated in an ocean anticyclonic eddy and in close proximity to Typhoon Kalmaegi, both before and after the typhoon's passage in 2014. Profiles of this Argo are also used to validate the vertical distribution of temperature and salinity from GLORYS12V1.

141   For this study, we also utilize in-situ data from a cross-shaped array consisting of five stations,

142   comprising five moored buoys and four subsurface moorings (refer to Fig. 1). More specific information

143   can be found in Zhang et al. (2016). To investigate the impact of the typhoon on a warm eddy, we select

144   the temperature and salinity data from Station 5, situates along the left track of Kalmaegi.

145   The wind speed data is sourced from the European Centre for Medium-Range Weather Forecasts

146   (ECMWF) ERA-Interim reanalysis assimilation dataset (https://apps.ecmwf.int/datasets/data/interim-

147   full-daily/levtype=sfc/ , last access: 5 January, 2023). This dataset is widely used for weather analysis

148   and numerical forecasting. The wind field data used in this study primarily focuses on the reanalysis data

149   of surface winds at a height of 10 meters above sea level for TCs. The selected data has a spatial

150   resolution of $1/4° × 1/4°$ and a temporal resolution of 6 hours, with four updates per day (00:00, 06:00,

151   12:00, and 18:00 UTC). The data utilize corresponds to September 2014.

152   The Global Ocean Reanalysis Product GLOBAL_REA- NALYSIS_PHY_001_030 (GLORYS12),

153   provides by the Copernicus Marine Environment Monitoring Service (CMEMS,

154   https://marine.copernicus.eu/, last access: 23 March, 2022) is used in this study too. This reanalysis

155   product utilized the NEMO 3.1 numerical model coupled with the LIM2 sea ice model, and forced with

156   ERA-Interim atmospheric data. The model assimilated along-track altimeter data from satellite

157   observations (Pujol et al., 2016), satellite sea surface temperature data from AVHRR, sea ice

158   concentration from CERSAT (Ezraty et al., 2007), and vertical profiles of temperature and salinity from

159   the CORAv4.1 database (Cabanes et al., 2012). The temperature and salinity biases were corrected using

160   a 3D-VAR scheme. The horizontal resolution is $1/12° × 1/12°$, and it has 50 vertical levels. The

161   temperature and salinity form 1 September to 30 September 2014 were chosen to study.

162   GLORYS12V1 is a widely used and applicable dataset, to evaluate its temperature profiles, the Argo

163   profiles and in-situ data of Station 5 were compared (Fig. 2). The GLORYS12V1 data exhibit good

164   agreement with Argo profiling floats, the maximum difference between them is less than 0.2℃, the Root

165   Mean Square (RMS) is 0.02. However, there are some discrepancies between the GLORYS12V1 and

166   the Station 5 data, with the largest difference occurring at the depths of 30 m (mixed layer) and 78 m

167   (thermocline), both differing by 0.6℃, while below 150 m, the difference is quite small. The RMS is

168   0.09. The RMS between GLORYS12V1 and Station 2 (Station 4) is 0.14 (0.10) (Figures not shown).

169   Because the GLORYS12V1 assimilates with Argo data and the vertical resolution of upper 100 m in

170   Argo profile is 5 m, but the vertical interval of buoy array is 20 m. Therefore, the large deviations exist

171   at mixed layer and thermocline during the typhoon in in-situ data of Station 5. Overall, GLORYS12V1

172   reproduces the observed ocean temperature accurately, it is reasonable to use it to investigate the vertical

173   response of anticyclonic eddies by Typhoon Kalmaegi.
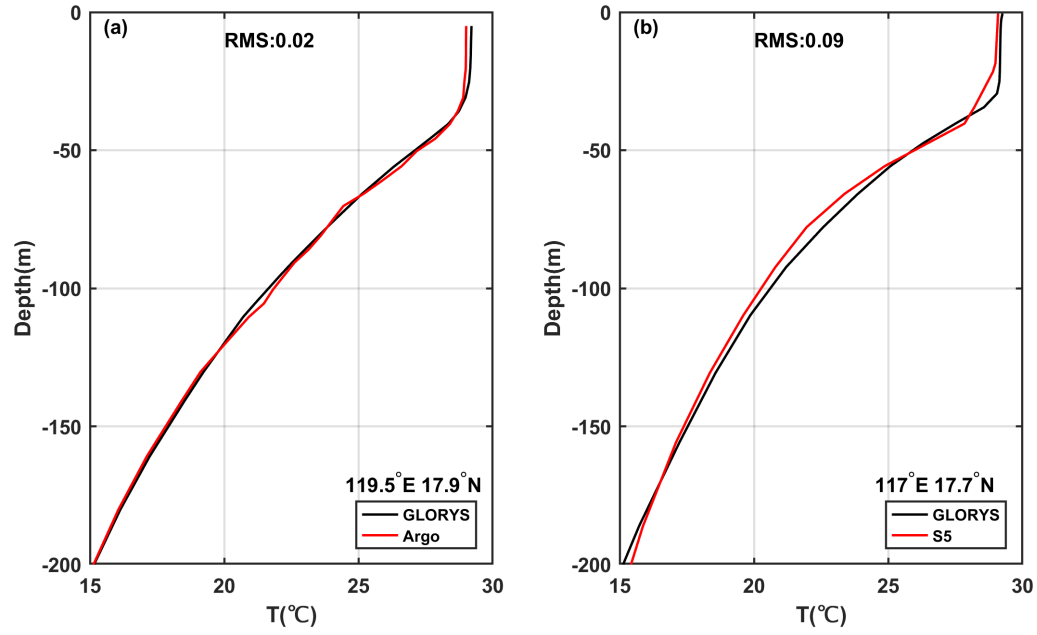
175 **Figure 2.** Evaluation of GLORYS12V1 data performance during September 2014. **(a)** Vertical monthly mean
176 temperature within the anticyclonic eddy AE2 (119.5°E 17.9°N) as measured by Argo float 2901469. **(b)**
177 Comparison of vertical monthly mean temperature recorded at Station 5 (117°E 17.7°N).

178 **2.2. Methods**

179 Vorticity is a vector that characterizes the local rotation within a fluid flow. Mathematically, it is
180 defined as the curl of the velocity vector. In most cases, when referring to vorticity, it specifically pertains
181 to the vertical component of the vorticity. It is calculated from:

182
$$\zeta = \frac{\partial v}{\partial x} - \frac{\partial u}{\partial y} \ . \tag{1}$$

183 u and v are the zonal (eastward) and meridional (northward) geostrophic velocities, respectively. They
184 are derived from altimeter sea level anomaly data (η):

185
$$u = -\frac{g}{f}\frac{\partial \eta}{\partial y} \ , v = \frac{g}{f}\frac{\partial \eta}{\partial x} \ . \tag{2}$$

186 Here, g is the acceleration of gravity, f is the Coriolis frequency. Vorticity is considered a
187 fundamental characteristic of mesoscale eddies, positive vorticity signifies cyclonic eddies, while
188 negative vorticity indicates anticyclonic eddies.

189 The Rossby number (Ro) is a dimensionless number describing fluid motion, and it is the ratio of
190 relative vorticity to planetary vorticity, reflecting the relative importance of local non-geostrophic motion
191 to large-scale geostrophic motion. The larger the Rossby number, the stronger the local non-geostrophic
192 effect, and the definition of this parameter is:

193
$$R_{\mathrm{o}} = \frac{\zeta}{f} \ . \tag{3}$$

194   Eddy Kinetic Energy (EKE) is a measure of the energy associated with mesoscale eddies, which

195   indicates the intensity of eddies. It is typically calculated using the anomalies of the geostrophic velocity:

196
$$EKE = \frac{1}{2}(u'^2 + v'^2) \ , \tag{4}$$

197   where u' represents the anomaly of the geostrophic zonal (eastward) velocity, v' represents the anomaly

198   of the meridional (northward) velocity.

199   To evaluate the impact of a typhoon on an anticyclonic eddy, the calculation begins with determining

200   the wind stress:

201
$$\vec{\tau} = \rho_a C_d U_{10} \overrightarrow{U_{10}} \ , \tag{5}$$

202   where ρ_a is the air density, assumed to be a constant value of 1.293 kg m^{-3}, U_{10} represents the 10-

203   meter wind speed. And C_d is the drag coefficient at the sea surface (Oey et al., 2006):

204
$$C_d \times 1000 = \begin{cases} 1.2 & U_{10} \leq 10m\ s^{-1} \\ 0.49 + 0.65U_{10} & 11 \leq U_{10} < 19m\ s^{-1} \\ 1.364 + 0.234U_{10} - 0.00023158U_{10}^2 & 19 \leq U_{10} \leq 100m\ s^{-1} \end{cases} . \tag{6}$$

205   The wind stress curl is calculated by (Kessler, 2006):

206
$$curl(\vec{\tau}) = \frac{\partial \tau_y}{\partial x} - \frac{\partial \tau_x}{\partial y} \ , \tag{7}$$

207   where τ_x and τ_y are the eastward and northward wind stress vector components, respectively. The curl

208   represents the rotation experienced by a vertical air column in response to spatial variations in the wind

209   field.

210   The Ekman pumping velocity (EPV) represents the ocean upwelling rate, which can be used to study

211   the contribution of typhoons to regional ocean upwelling. Positive means upwelling, negative represents

212   downwelling:

213
$$EPV = curl(\frac{\vec{\tau}}{\rho f}) \ , \tag{8}$$

214   where the wind stress is obtained from Eq. (7), ρ is seawater density, the value is 1025 kg m^{-3}, and f

215   is the Coriolis frequency.

216   The buoyancy frequency is a measure of the degree to which water is mixed and stratified. In a stable

217   temperature stratification, the fluid particles move in the vertical direction after being disturbed, and the

218   combined action of gravity and buoyancy always makes them return to the equilibrium position and

219   oscillate due to inertia. When N^2 < 0, the water is in an unstable state:

220
$$N^2 = -\frac{g}{\rho}\frac{\partial \rho}{\partial z} \tag{9}$$

221   where ρ is seawater density, g is the acceleration of gravity, and z is the depth.

3. Results

3.1. Typhoon and pre-existing eddies in the NSCS

3.1.1. Track of Typhoon Kalmaegi and tropical storm Fung-wong

Typhoon Kalmaegi strengthens into a typhoon by 1200 UTC on 13 September and emerged over the warm waters of the Northern South China Sea (NSCS) by 1500 UTC on 14 September, with maximum sustained winds of 33 m.s^{-1} (Fig. 3-4). During this period, the NSCS experiences predominantly weak vertical wind shear and is characterized by multiple anticyclonic warm eddies (Fig. 3). Subsequently, Typhoon Kalmaegi undergoes two rapid intensification phases between 15 and 16 September. The first intensification occurs at 0000 UTC on 15 September, propelling Kalmaegi to category 1 status with surface winds surpassing 35 m.s^{-1}. By 1200 UTC on 15 September, Kalmaegi experiences a second, even more rapid intensification, with winds reaching 40 m s^{-1} in less than 12 hours. Throughout this intensification stage, Kalmaegi encounters two warm eddies: anticyclonic eddy AE1, is positioned to the left of the typhoon's path, with its core situates on the periphery of the typhoon's two-times maximum wind radius (Fig.3c-d). AE1 has a lifespan of 105 days from 26 June to 8 October and is positioned at 17°N-20°N, 113°E-116°E. AE2 precisely intersecting with the typhoon's trajectory, and its core nearly coincides with the maximum wind radius of the typhoon (Fig.3b-d).. It has a lifespan of 89 days from 24 August to 20 November and is located at 17°N -19°N, 118°E -120°E. Kalmaegi makes landfall on Hainan Island at 0300 UTC on 16 September, with a minimum central pressure of 960 hPa and a maximum wind speed of 40 m.s^{-1}. After landfall, Typhoon Kalmaegi gradually weakens and dissipates. During its crossing of the NSCS, the five mooring stations are affected. Stations 1 and 4 are on the right side of Typhoon Kalmaegi's track, while Stations 2 and 5 are on the left side. Unfortunately, the wire rope of the buoy at Station 3 is destroyed by Kalmaegi, resulting in missing data from 15 September. Among the stations, Station 5 is on the left of typhoon track and outside AE2, so its data is used in our study.

Tropical storm Fung-wong initially moves quickly in a northwest direction after formation. On 19 September, it enters the Luzon Strait and decelerates. It makes landfall in Taiwan on the 21 September and subsequently lands in Zhejiang on the 22 September before gradually dissipating. When crossing the Luzon Strait at 1200 UTC on 19 September, anticyclonic eddy AE2 is on the left side of Fung-wong, with a distance of just over 100 km from its center.
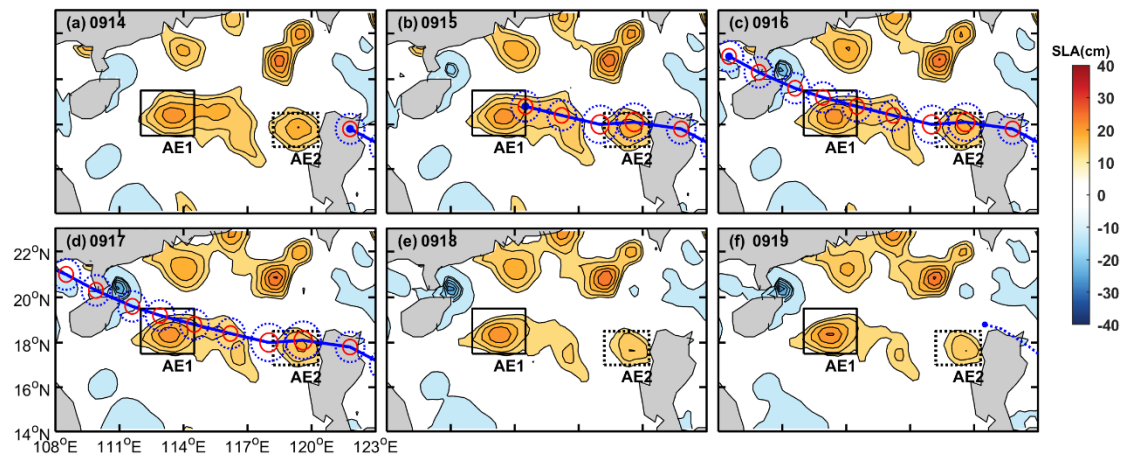
Figure 3. The variations in sea level anomaly before and afterTyphoon Kalmaegi moved over the anticyclonic eddies
AE1 and AE2 between 14 September and 19 September **(a-f)**. The black solid rectangle represents the area of AE1,
while the black dashed rectangle represents the area of AE2. The blue solid line depicts the path of Typhoon
Kalmaegi, the solid red and dashed blue circles are the one- and two-times maximum wind radius of the typhoon,
while the blue dotted line in **(f)** is the path of tropical storm Fung-wong (best-track data sourced from CMA).

3.1.2. Eddy characteristics distribution

Satellite SLA measurements have proven to be highly effective and widely used for identifying and
quantifying the intensity of ocean eddies (Li et al., 2014). In Fig. 3, two warm eddies with clear positive
(>13 cm) SLA are observed along the Typhoon Kalmaegi's track. During the period of 15 to 16
September, the typhoon passes over two warm anticyclonic eddies, AE1 and AE2.Before the typhoon,
AE1 is the most prominent eddy in the SCS, with an amplitude of 23.0 cm, and a radius of 115.5 km.
AE2, locates west of Luzon Island, exhibites an amplitude of 21.2 cm, with a radius of approximately
65.5 km. Tracing back to 2 months (figure is not shown), AE1 propagates slowly westward with about
0.1 m.s^{-1}, while AE2 is generated on 24 August. During 14 to 19 September, the amplitude of AE1
increases 1.3 cm. The area of the AE1 decreases by approximately 31% from 1.3×10^5 km^2 to 9.1×10^4
km^2 and splits into two eddies. When Typhoon Kalmaegi crosses the core of AE2 at 1500 UTC on 14
September, and tropical storm Fung-wong moves over the northeast of AE2 at 1200 UTC on 19
September, the amplitude decreases by 3.1 cm. The area of the AE2 decreases by approximately 36%
from 4.2×10^4 km^2 to 2.7×10^4 km^2.

Because of intense solar radiation in September, the SST in the SCS is generally above 28.5℃ prior
to the arrival of Typhoon Kalmaegi (Fig. 4a). As a fast-moving typhoon with a mean moving speed of
over 8 m.s^{-1}, Kalmaegi induces a larger cooling area and intensity on the right side of its path compared
to the left side (Price, 1981). During the passage of Kalmaegi, the lowest SST on the right side of typhoon
decreases to 27.2℃. Even after the typhoon has passed, a cold wake could still be observed on the right
side of its path, persisting for over a week (Fig. 4c).

Mesoscale eddies, due to their special thermodynamic structure and varying positions in relation to
the TC, can modulate distinct sea surface temperature changes and exhibit different characteristics. The
pre-existing warm eddy AE1 begins to cool down before Kalmaegi reached the NSCS, dropping to

279   28.4°C on 14 September. During this period, the mean SST within AE1 increases slightly to 28.6 °C (Fig.

280   5a). However, as cooler water from the right side of the typhoon track is subsequently advected into the

281   AE1 region (Fig. 4c), the SST decreases and reaches 28.0 °C on September 19, which is 0.4°C lower

282   than that before the typhoon. The average SST drop in AE2 is relatively evident, with SST starting to

283   decline before 14 September and reaching its lowest temperature (28.1°C) on 15 September, 0.6 °C lower

284   than that before the typhoon (Fig. 5e). On 16 September, the SST within AE2 begins to recover, but it

285   starts to cool again on 18 September due to the influence of Fung-wong.

286   Then we compare the Ro and EKE of AE1 and AE2 before, during and after typhoon. Before being

287   influenced by the typhoon, the warm eddy AE1 exhibits a more scattered distribution of negative Ro due

288   to its edge structure, and the EKE values at the eddy boundary are relatively high (Fig. 4d, g). As the

289   typhoon passes through the eddy, the Ro and EKE of AE1 startes to increase. On 19 September, the

290   average Ro within AE1 reaches a value of -8.2×10^{-2}, at the same time, the average EKE increases to its

291   maximum value of 325.0 $cm^2.s^{-2}$. The variation trend of R_O and EKE within the eddy is consistent,

292   increasing from the passage of the typhoon and starting to recover on 20 September (Fig. 5b-c). This

293   indicates that although the area of the warm eddy AE1 decreased under the influence of the typhoon, its

294   intensity increases. On the other hand, for warm eddy AE2, both R_O and EKE decreases after the typhoon

295   passage, with the Ro decreasing to -4.5×10^{-2} on 17 September and the EKE decreasing to 152.0 $cm^2 \ s^{-2}$

296   on the 19 September, followes by a recovery (Fig. 5f-g). Unlike AE1, AE2 weakenes in intensity under

297   the influence of the typhoon.

298   During the passage of the typhoon, enhances mixing driven by wind stress and increases vertical

299   shear result in a deepening of the MLD, which further strengthens the mixing between the deep cold

300   water and the upper warm water (Shay and Jaimes, 2009). To avoid a large part of the strong diurnal

301   cycle in the top few meters of the ocean, 10 m is set as the reference depth (De Boyer Montégut, 2004).

302   A 0.5 °C threshold difference from 10 m depth is calculated and defines as the MLD (Thompson and

303   Tkalich, 2014). Prior to the influence of typhoon Kalmaegi, the MLD in the AE1 and AE2 regions is

304   deeper (Fig. 4j), with the average MLDs of 32 m and 33 m, respectively. Starting from 14 September,

305   the MLDs are influenced by typhoon Kalmaegi, with the MLD of AE1 deepening to 37 m and that of

306   AE2 increasing to 41 m, representing a deepening of 5 m and 8 m, respectively (Fig. 5d, h).

307   Overall, Typhoon Kalmaegi likely exerts distinct impacts on the two warm eddies. Despite both AE1

308   and AE2 experiencing a decrease in their respective areas by approximately one-third, accompanies by

309   deepening of the MLD, the amplitude of SLA within AE1 increases by 1.3 cm, whereas AE2 witnesses

310   a decrease of about 3.1 cm in its amplitude. Furthermore, the SST, Rossby number and EKE within AE1

311   and AE2 exhibites contrasting patterns.
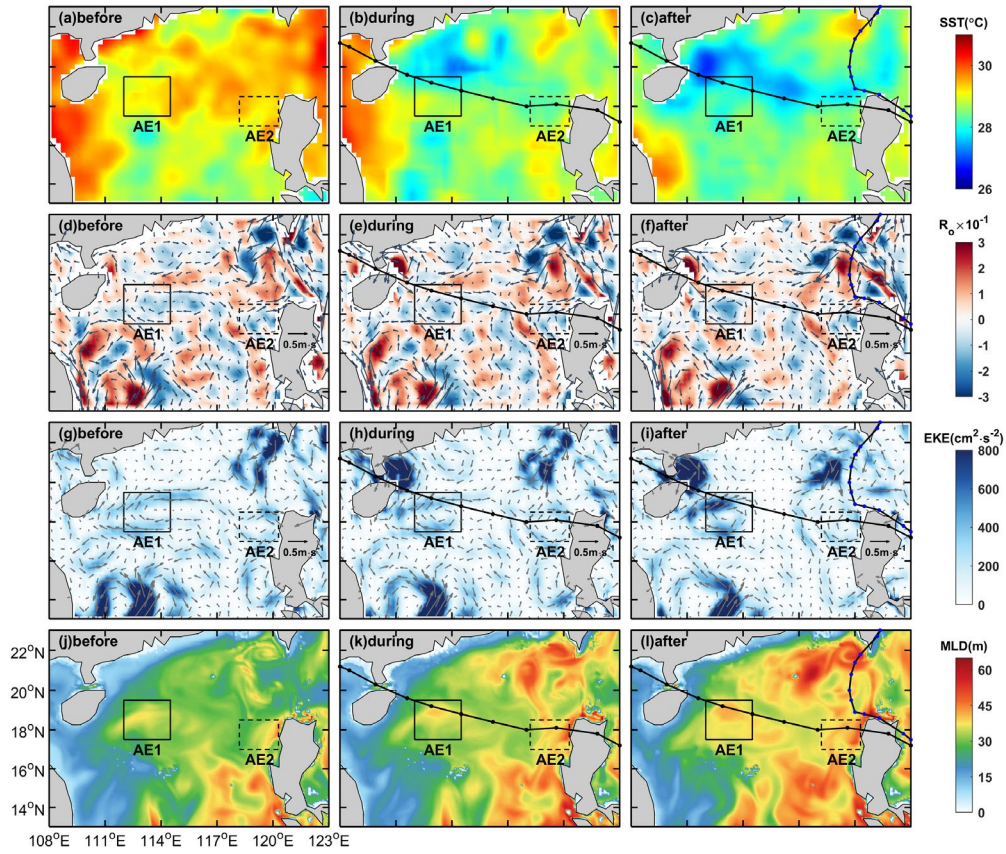
313 **Figure 4.** The spatial distribution of SST, R_o, EKE, and MLD before, during and after the passage of TCs. The

314 time periods of 10-13, 15-16 and 19-22 September are designated as stages before, during and after Kalmaegi,

315 respectively. The path of Typhoon Kalmaegi is depicted by a black solid line with black dots, while the path of

316 tropical storm Fung-wong is represented by a black solid line with blue dots in the third column. The solid and

317 dashed boxes correspond to AE1 and AE2, respectively.
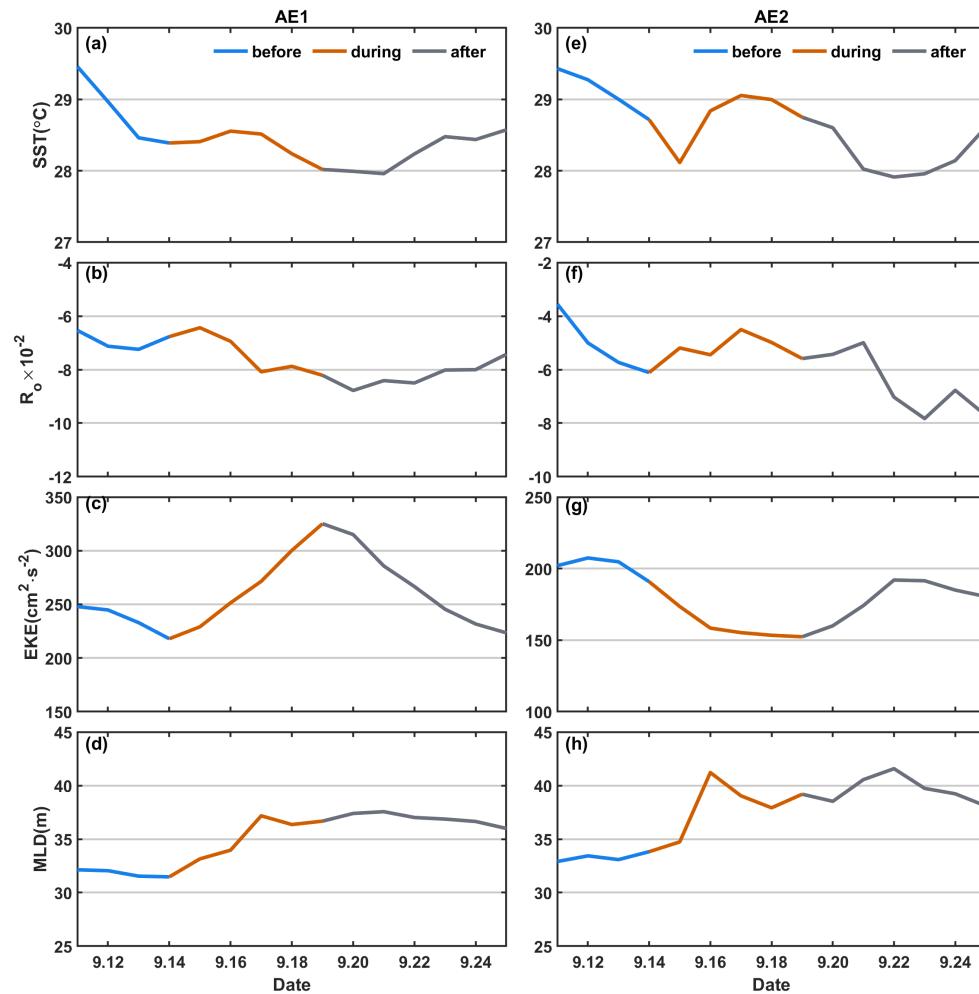
Figure 5. The time series of sea surface temperature (SST), R_o, eddy kinetic energy, and mixed layer depth (MLD) within the warm eddies' regions (black solid and dashed boxes in Fig. 4). The first column is variables of AE1, the second column is for AE2.

3.2 Upper-ocean vertical thermal and salinity structure of eddies

We conductes further analysis on the vertical temperature and salinity structure of the warm eddies AE1 and AE2 before and after the Typhoon Kalmaegi using GLORYS12V1 data. During the typhoon's passage on 15 September, the temperature above the MLD within AE1 increases by approximately 0.1 °C, while the salinity decreases by 0.02psu (Fig. 6). Below the MLD, the temperature shows a significant increase, reaching a maximum temperature rise of 1.3 °C. Correspondingly, the salinity below the MLD exhibits a decrease of 0.05 psu. Vertical temperature on Kalmaegi's arrival day shows warm pattern from surface to 200 m, the salinity shows "fresher-saltier" pattern. These changes lead to a deepening of the isodensity by 15 m and a decrease in buoyancy frequency N^2 (Fig. 7a-b), indicating convergence and downwelling within the centre of the warm eddy AE1. The near-inertial waves propagates downward from surface to 200m from this period (Zhang et al, 2017). The transfer of energy from anticyclonic eddy to near-inertial waves is the main reason for the downward progpation and longtime perisistence of near-inertial energy (Chen et al, 2023).

After 15 September, the temperature above the MLD decreases, and the salinity shows an increase (Fig. 6a-b), resulting in the uplift of the 1021 kg.m^{-3} isodensity to the sea surface (Fig. 7a-b). The subsurface warming and salinity reduction gradually weakens after the Typhoon Kalmaegi but persists for about a week after the typhoon's passage until 22 September. During this period, vertical temperature pattern becomes "cool-warm" at the center of AE1, and the salinity distribution pattern becomes "saltier-fresher-saltier". This persistence can be attributed to the intensified stratification around the MLD, with N^2 around 9.0×10^{-4}s^{-2} (Fig. 7b). The increased stability inhibits vertical mixing, restrains the exchange of heat and salinity, and leads to smoother density gradients above the MLD (Fig. 7a).

The vertical temperature and salinity structure of AE2 exhibits an opposite trend. During the typhoon passage on 15 September, AE2 also experiences a cooling trend of 0.2 °C, with a decrease in salinity of 0.04 psu above the MLD. Below the MLD, the temperature shows a consistent decrease, with a change of less than 0.5 °C within the subsurface. Correspondingly, the salinity exhibits an increase of approximately 0.08 psu (Fig. 6c-d). The slightly upward shift of the isodensity (Fig. 7c) suggests the possibility of cold-water upwelling induced by the suction effect of the typhoon. The temperature decreases and salinity increases below the MLD are primarily driven by upwelling processes.

Furthermore, when the tropical storm Fung-wong passes through AE2 on 19 September (dashed line in Fig. 6c-d), the decreasing trend of subsurface temperature becomes more pronounced, and the subsurface salinity exhibits a significant increase. AE2 is more significantly influenced by tropical storm Fung-wong. It presents stable stratification with N^2 around 8.4×10^{-4}s^{-2} at a depth of 42 m, creating a barrier layer that prevents the intrusion of high-salinity cold water from the lower layers into the mixed layer (Yan et al., 2017).
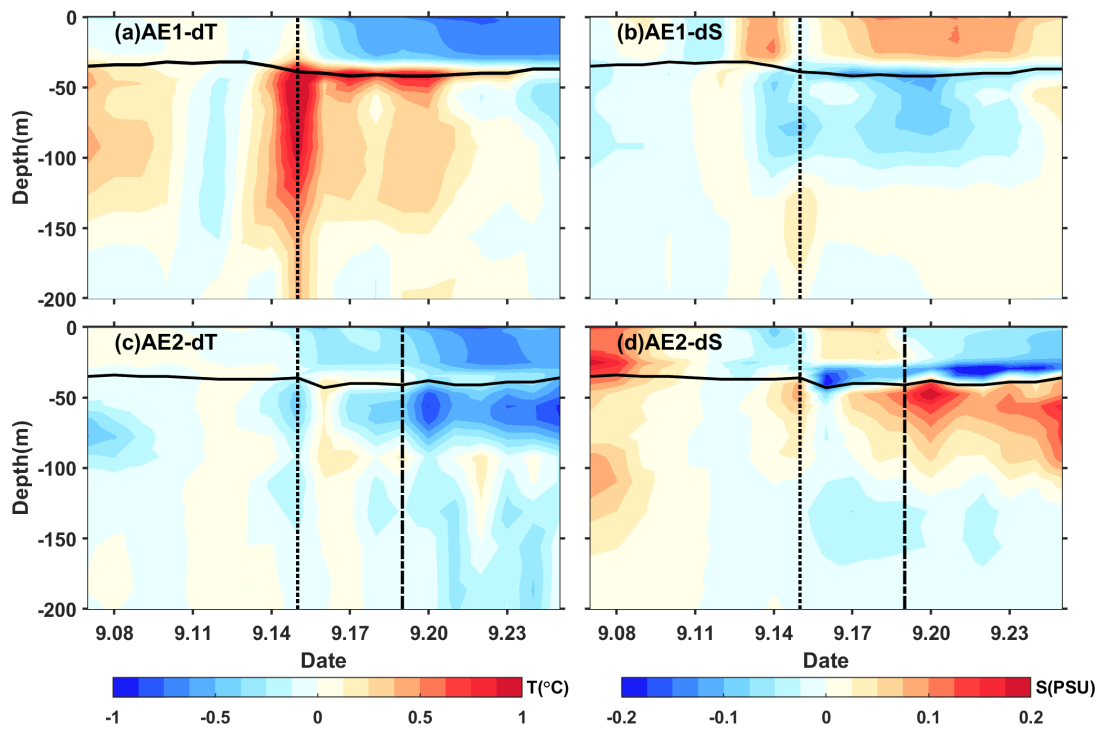
Figure 6. The timeseries of vertical temperature and salinity anomalies in the center of AE1(a,b) and AE2 (c,d). The anomalies were calculated relative to the average value of 10-13 September. The vertical black dotted line indicates theTyphoon Kalmaegi's passage, while the vertical black dashed line represents the passage of tropical storm Fung-wong. The black solid line is the MLD.
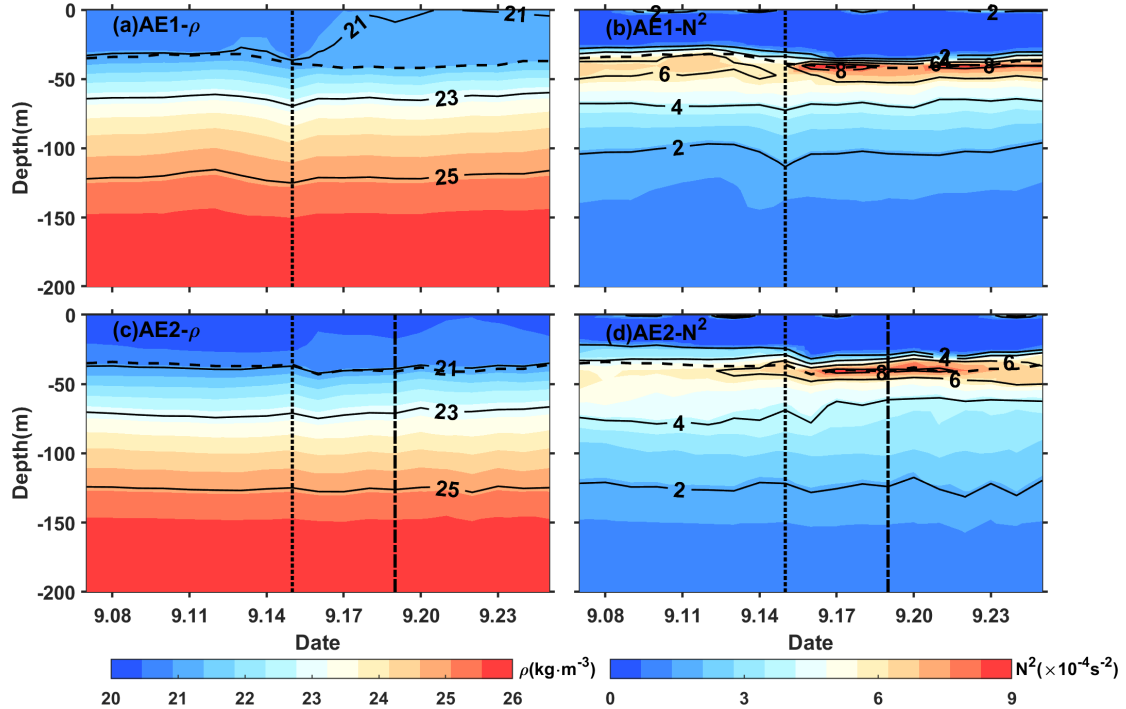
Figure 7. Same as Fig. 7, but for density and buoyancy frequency (N^2).

3.3 Comparison of the response between eddies and non-eddies areas

To investigate the contrasting response of warm eddies and the non-eddies background to Typhoon Kalmaegi, we conduct a comparative analysis of vertical temperature and salinity profiles in these two areas. Unfortunately, there is no Argo data around AE1, therefore, we examine data from Argo 2901469, which is located within AE2 during the period from 11 to 19 September. The temperature and salinity data from Station S5 is considered as the background, with S5 locates at a distance of 246 km from AE2's center on 15 September (Fig. 1). These profiles are categorized into three periods: pre-typhoon (11 September), during-typhoon (15 September), and post-typhoon (19 September).

At depths above 40m, both inside and outside of AE2 experiences a decrease in temperature, with a cooling of less than -1.0℃. Four days after the typhoon passage (19 September), the cooling persists inside and outside the eddy, with the cooling being more pronounced outside AE2, showing a decrease of 1.2 ℃ (Fig. 8c). The salinity within AE2 initially increases by 0.15 psu from the pre-typhoon stage to the during-typhoon stage and then decreases by 0.09 psu after the typhoon passage (Fig. 8d). While the salinity at Station 5 shows a similar pattern in pre-typhoon and during-typhoon stage, it increases by 0.05 psu after the typhoon. Two possible processes can explain the difference in salinity trends inside and outside AE2. First, during the pre-typhoon to typhoon stage, the entrainment within AE2 may have brought the subsurface water, which is saltier, up to the surface, resulting in an increase in salinity. The

second process is related to the typhoon-induced precipitation after the typhoon passage, which lead to a decrease in salinity. Strong stratification have contributed to the persistence of saltier subsurface water. While at S5, the increase in salinity is relatively minor only increased slightly.

On 15 September, the subsurface layer at 45 m to 100 m is affected by the cold upwelling, which is caused by the typhoon, resulting in a cooling and increased salinity within AE2. As the forcing of Typhoon Kalmaegi diminishes, the upper layer of seawater begins to mix, and influences by the downward flow of the eddy itself, warm surface water is transported to the subsurface layer. Four days later, a warming phenomenon occurs, with the maximum warm anomaly of 1.2 ℃ observes at a depth of 75 m (Fig. 8a). The mixing effect outside the eddy is not significant, resulting in a slight subsurface warming of approximately 0.2 ℃, with no significant changes in salinity. However, on 19 September, a maximum cold anomaly of -1.2℃ is observed at a depth of 60 m, corresponding to the maximum salinity anomaly of 0.13 psu (Fig. 8c-d). Below 100 m, AE2 experiences a temperature increase of 0.5 ℃ and a slight decrease in salinity of 0.04 psu. On 19 September, the temperature and salinity within AE2 shows little change. However, outside the eddy, a different response is observed. On 19 September, a cooling trend is observed throughout the water column, within a range of 0.2 ℃, accompanies by a noticeable increase in salinity (Fig. 8c, d), within a range of 0.06 psu. This indicates that the typhoon causes a significant upwelling outside the eddy region.
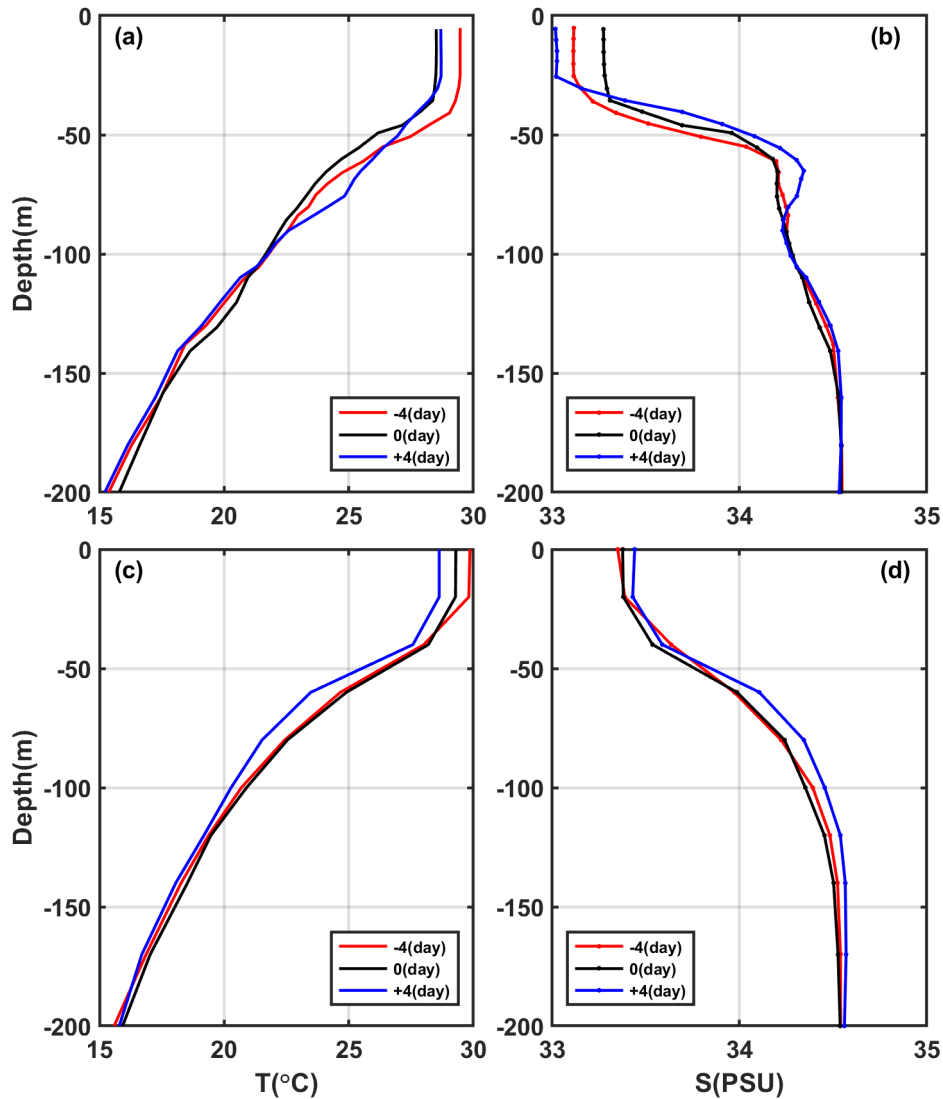
Figure 8. (a-b) the vertical profile of temperature and salt inside the eddy (Argo 2901469), **(c-d)** the vertical profiles of temperature and salt outside the eddy (S5). The red, black and blue lines represent pre-typhoon, during-typhoon and post-typhoon stages.

Based on Argo profiles and S5 data, the upper ocean above 200 m inside and outside AE2 responds differently to the forcing of the typhoon. In the upper layer (0-40 m), cooling is observed both inside and outside the eddy, and it lasts for a longer duration. In the subsurface layer (45-100m), after the passage of the typhoon (19 September), there is a strong cooling outside the eddy, while warming occurs within AE2. Zhang (2022) points out that the sea temperature anomalies mainly depend on the combined effects of mixing and vertical advection (cold suction). Mixing causes surface cooling and subsurface warming, while upwelling (downwelling) leads to cooling (warming) of the entire upper ocean. The temperature anomaly in the subsurface layer depends on the relative strength of mixing and vertical advection, with cold anomalies dominating when upwelling is strong, and downwelling amplifying the warming anomalies caused by mixing. Therefore, due to the strong influence of upwelling outside the eddy, the temperature profile of the entire water column shifts upwards, resulting in cooling of the entire upper ocean. On the other hand, influences by the downwelling associates with the warm eddy itself, a warming

414   anomaly of 1.2 °C is observed in the subsurface layer. Compares to region AE2, the cold suction effect

415   causes by the Typhoon Kalmaegi is still evident in the non-eddy area.

416   In the following sections, we delve into the underlying reasons behind these different responses of

417   AE1 and AE2 to Typhoon Kalmaegi.

418

4. Discussion

420   The EPV is very small before the typhoon, measuring less than 0.5×10^{-5} m.s^{-1} in both AE1 and AE2.

421   However, during 15-16 September (Fig. 9c-f), when typhoon crosses the NSCS, the EPV undergoes

422   significant changes. Its absolute value increases to over 1.5×10^{-4} m.s^{-1} within both AE1 and AE2. AE1

423   consistently exhibits a predominantly negative EPV during most of this period. Consequently, during

424   Typhoon Kalmaegi, the negative EPV facilitates downwelling and convergence (Jaimes and Shay, 2015),

425   leading to a warmer and fresher subsurface layer in AE1 (Fig. 6 a-b).

426   On the other hand, AE2 displays a more fluctuating pattern. It is positive on 14 September, shows

427   both positive and negative values at 0000 UTC on 15 September, and remains mainly negative from 15

428   to 16 September, and eventually returning to positive, reflecting a continuously fluctuating process. The

429   positive EPV in AE2 contributes to the influx of colder subsurface water into the upper layers, resulting

430   in surface and subsurface water cooling and an increase in salinity in the subsurface (Fig. 6c-d).

431   Correspondingly, the variations in Ekman layer depth (D_E) with the typhoon's passage are similar to EPV,

432   as shown in Fig. 10. When Kalmaegi approaches at 0000 UTC on 14 September, the mean D_E within

433   AE1 is only 21 m, while in AE2, it is 114 m. This indicates that AE2 has already been influenced by

434   Typhoon Kalmaegi. Subsequently, the depth of the DE within AE2 sharply deepens, reaching its

435   maximum depth of 241 m at 0000 UTC on 15 September, coinciding with the proximity of Typhoon

436   Kalmaegi's center to AE2.. As Kalmaegi moves northwest, the D_E within AE1 achieves its maximum

437   depth of 262 m at 0000 UTC on 16 September. The trends of D_E within AE1 and AE2 are nearly

438   consistent, but AE1 lags behind AE2 by one day. Starting from 15 September, D_E within both AE1 and

439   AE2 gradually shallows, reaching a minimum D_E of 60 m. This value is 28 m higher than before the

440   typhoon, indicating the lingering effects of the typhoon through wind. For AE2, D_E reached its minimum

441   of 45 m at 0000 UTC on 18 September, later gradually increasing under the influence of tropical storm

442   Fung-wong.
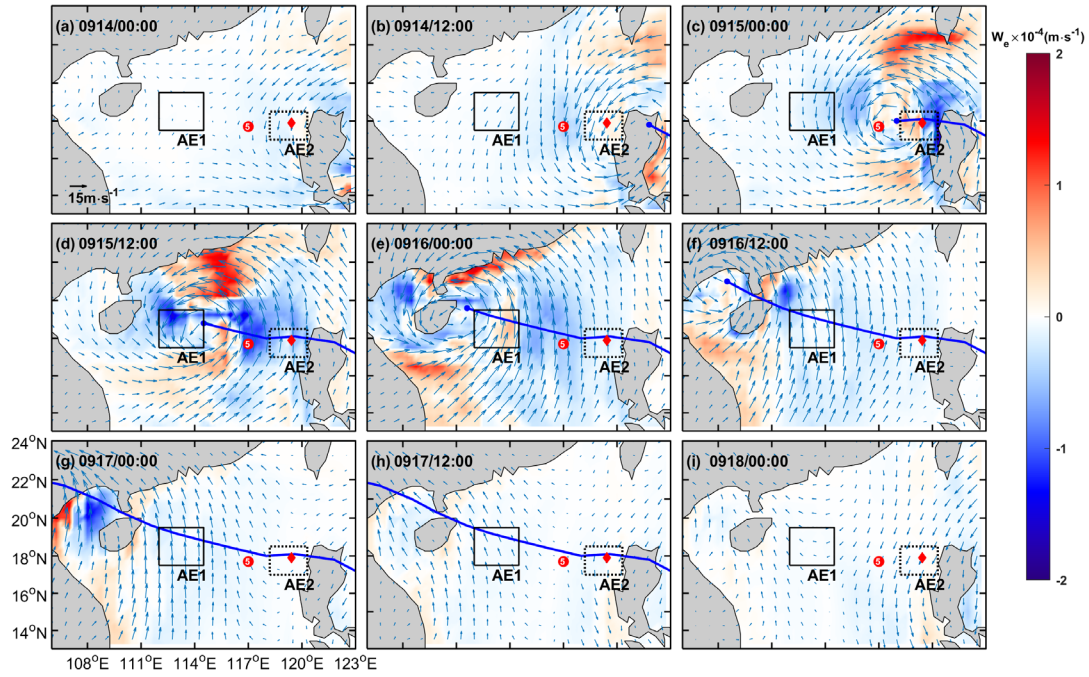
444 **Figure 9.** Ekman Pumping Velocity (EPV) from 14 September to 18 September **(a-i)**. The color represents the EPV,
445 the blue solid line is the path of Kalmaegi, the red dot and diamond are the positions of Station 5 and Argo 2901469
446 on 15 September, respectively.
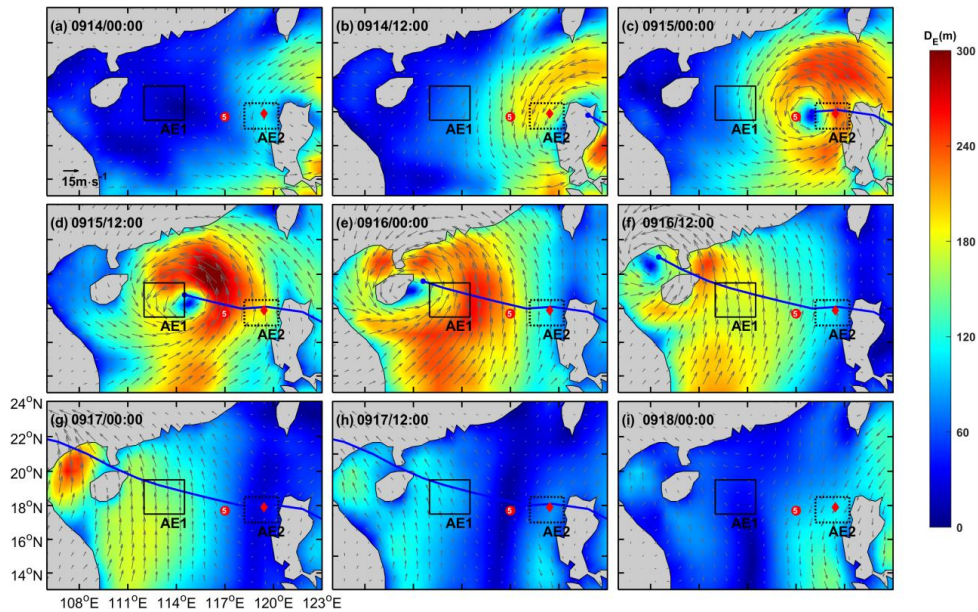
448 **Figure 10.** Ekman layer depth (D_E) from 14 September to 18 September **(a-i)**. The color represents the D_E, the blue
449 solid line is the path of Kalmaegi, the red dot and diamond are the positions of Station 5 and Argo 2901469 on 15
450 September, respectively.

451   After traversing the warm ocean characteristics of AE2, Typhoon Kalmaegi strengthens, resulting in
452 a reduction of the maximum wind radius. As it passed through AE1, the maximum wind radius is 35 km.
453 Notably, the center of AE1 is located outside the typhoon's two-times maximum wind radius,
454 approximately 104 km away from the typhoon center (Fig. 3). As mentioned earlier, strong upwelling
455 occurs within two-times maximum wind radius, while weak subsidence exists in the vast area outside

456 the upwelling region (Jaimes and Shay, 2015). Hence, the hypothesis presents here suggests that the

457 observed intensification of AE1 on the left side of the typhoon track is more likely attributed to the

458 negative wind stress generates outside the maximum wind radius, driving the enhancement of

459 downwelling in the pre-existing anticyclonic feature in the ocean. Starting from 15 September, a

460 significant positive sea level anomaly (SLA) to the west of 113.5°E becomes evident, intensifying and

461 reaching its maximum on 20 September (Fig. 11a). This strengthening aligns with the increase in the

462 amplitude of the warm core of the eddy AE1. A comparison with the wind stress curl anomaly (Fig. 11b)

463 reveals that between 15 to 16 September, as the Typhoon Kalmaegi moves over the section at 18.2°N,

464 specifically to the west of 113.5°E, it exhibits strong negative wind stress curl anomalies, with a

465 maximum intensity of -3×10^{-6} N.m^{-3}. The negative wind stress curl induces by the typhoon results in

466 favourable surface ocean currents that further enhances the clockwise rotation of the warm eddy. The

467 negative wind stress curl anomaly results strong downwelling currents, inputting negative vorticity into

468 AE1, leading to its intensification (Fig. 4b-c), as indicates by the enhanced positive SLA (Fig. 11a).

469 Conversely, the region to the east of 113.5°E along the section exhibited negative SLA anomalies. This

470 weakening is consistent with the previous observations of the intensified warm core and decreased eddy

471 area.
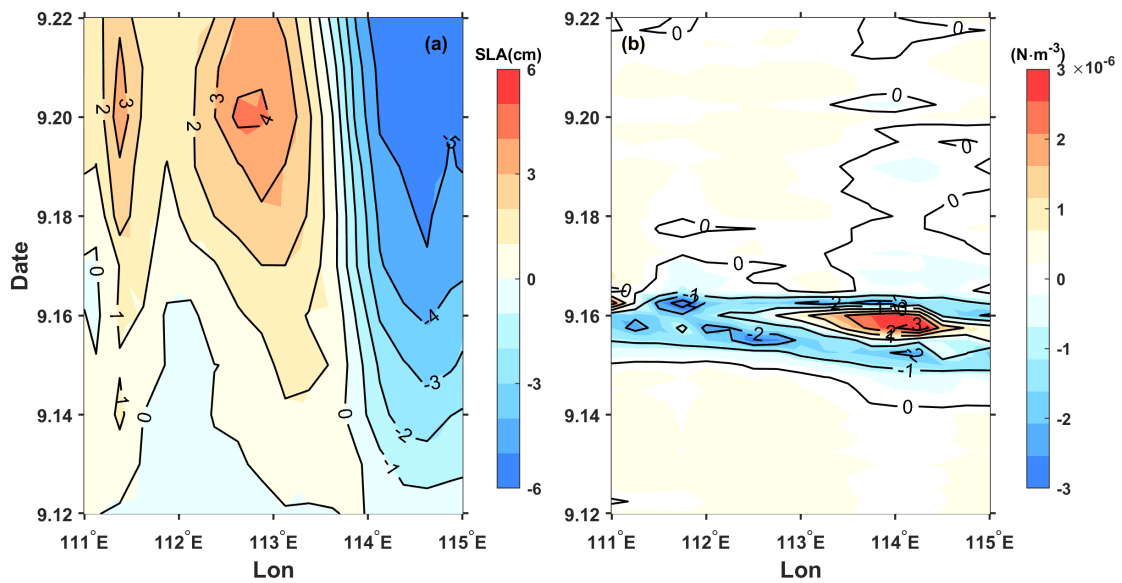
473 **Figure 11.** The time/longitude plots of **(a)** SLA anomaly (cm) and **(b)** wind stress curl (N.m^{-3}) anomaly at the central

474 section of AE1 (18.2 °N). The anomalies were calculated relative to the average value of 10-13 September.

475 The response of AE2 differs from that of AE1 mainly because AE2 is quite near the Typhoon

476 Kalmaegi's track. As the typhoon passes through AE2, the maximum wind radius is 48 km. AE2 is

477 merely 26 km away from the typhoon center, essentialy falling within two-times the maximum wind

478 radius of the typhoon (Fig. 3). The significantly positive wind stress curl at the typhoon center induces

479 upwelling and positive vorticity downward into the eddy (Huang and Wang, 2022), noticeably weakens

480 the eddy, corresponding to the decrease in SLA (Fig. 12a). Furthermore, bases on the meridional isotherm

481 profiles of the eddy center at three periods, it can be observed that during the passage of Typhoon

482 Kalmaegi (15 September), the isotherms in the AE1 region exhibit significant subsidence (Fig. 13a),

483 while in the AE2 region, the isotherms show uplift (Fig. 13b). This result aligns with the earlier

484 observation that the convergence and subsidence within the warm eddy AE1 are enhances by the

485 influence of the wind stress curl induced by the typhoon, while the intensity of AE2 is weakened.
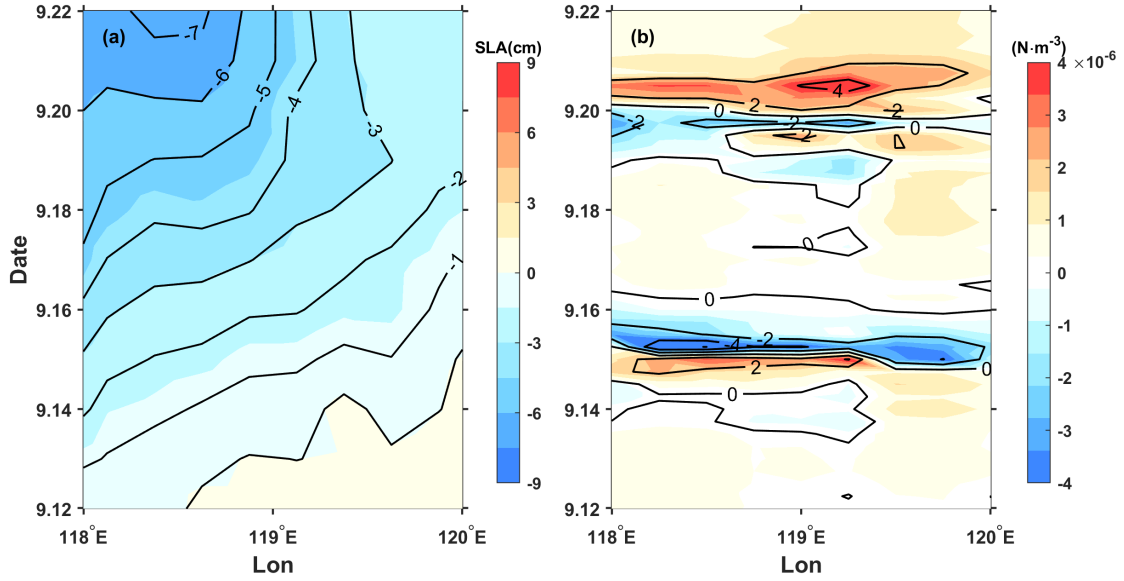
487 **Figure 12.** Same as Fig.10, but for AE2(17.9 °N)**.**

488   From the above, the relative position of eddies and the typhoon can influence the response of the

489 eddies (Lu et al., 2020). The warm eddy AE1, locates on the left side of the typhoon track, is not

490 weakened by the strong cold suction effect causes by the typhoon Kalmaegi. Instead, it is strengthened

491 due to the stronger negative wind stress curl generated by the typhoon.

492   To understand the work done by the Typhoon Kalmaegi on the eddies in the ocean, we estimate the

493 total work inputted into the ocean current u_c using the previously calculated wind stress (Liu et al.,

494 2017):

495
$$W = \int \vec{\tau} \cdot \overrightarrow{u_c}\, dt \quad . \tag{10}$$

496 Here, we select the region near the typhoon track where the wind speed exceeds 17 m.s^{-1} as the typhoon

497 forcing region to understand the energy input by the typhoon to the warm eddy (Sun et al., 2010). The

498 forcing duration over the ocean in the typhoon-affected region and the work done by the typhoon on the

499 surface current are shown in Fig. 13. When the angle between the wind and the ocean current is acute,

500 the typhoon does positive work on the ocean current. Conversely, when the angle is obtuse, the typhoon

501 does negative work on the ocean current. It is evident that the region with the maximum forcing duration

502 by the typhoon on AE1 corresponds to the area where the typhoon clearly does positive work on the

503 ocean current, accumulating a work done exceeding 8 KJ m^{-2}. This acceleration of the flow velocity in

504 the eddy results in convergence within the eddy and an increase in SLA, leading to the strengthening of

505 AE1. On the other hand, the forcing duration by the typhoon on AE2 is smaller, and the typhoon does

506 negative work on the ocean current in most areas, with a cumulative work done within -5 KJ m^{-2}, causing

507 the flow velocity within the AE2 to decelerate.
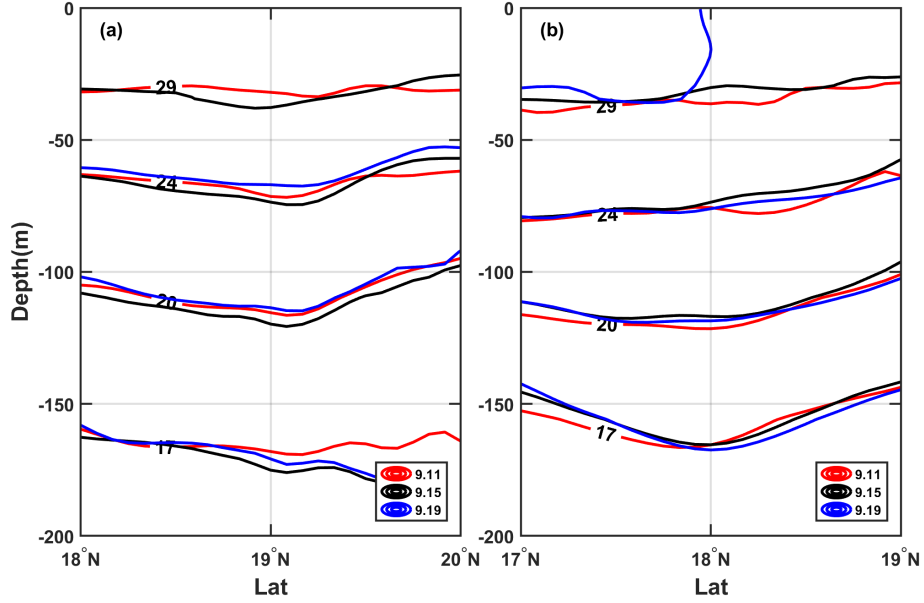
Figure 13. The meridional isotherm profiles of AE1 **(a)** and AE2 **(b)** before (11 September), during (15 September) and after (19 September) typhoon Kalmaegi.
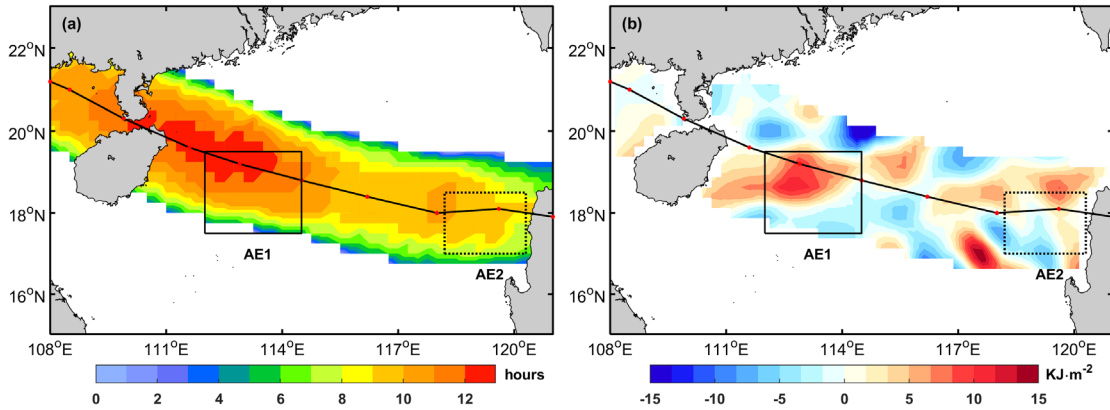
Figure 14. **(a)**: the forcing time (unit: hours) of the typhoon; **(b)**: the input work (unit: KJ. m^{-2}) of the typhoon to the current.

5. Summary

Based on multi-satellite observations, on-site measurements, and numerical model data, we have gained valuable insights into the response of warm eddies AE1 and AE2 in the northern South China Sea to Typhoon Kalmaegi. Both horizontally and vertically, these eddies display distinct differences. Horizontally, we observe a reduction of areas by approximately 31% (AE1) and 36% (AE2). AE1, positions on the left side of the typhoon's track, strengthens with amplitude, R_O and EKE increasing by 1.3 cm, 1.4×10^{-2} and 107.2 cm^2.s^{-2} after the typhoon passed. In contrast, AE2, which intersects with the typhoon's track, weakens with amplitude, R_O and EKE decreasing by 3.1 cm, 1.6×10^{-2} and 38.5 cm^2.s^{-2}, respectively. Vertically, during the typhoon's passage, AE1 experiences intensified converging subsidence flow at its center, leading to an increase in temperature and a decrease in salinity above 150 m. This response is more pronounced below the MLD (1.3°C) and persists for about a week after the

typhoon. On the other hand, AE2 exhibits cooling above the MLD, accompanies by a decrease in salinity, as well as a subsurface temperature drop and salinity increase due to the upwelling of cold water causes by the typhoon's suction effect. The subsurface cooling and salinity increase in AE2 are further influenced by Typhoon Fung-wong. Additionally, from the temperature vertical profile of Argo and in-situ arrays, on 19 September, it can be seen that the non-eddy region also experiences significant cooling, with a prominent cooling center observes at a depth of 60 m (-1.2 ℃). The warm eddy AE2, influences by its own downwelling, exhibites enhanced mixing effects, resulting in a subsurface warm anomaly of 1.2 ℃.

Further analysis reveals that the different responses of the warm eddies can be attributed to factors such as wind stress curl distribution, which are influenced by the relative position of the warm eddies and the typhoon track. The wind stress curl induces by the typhoon plays a crucial role in shaping the response of the warm eddies. AE1, locates on the left side of the typhoon's path, experiences prolonged forcing from the typhoon, resulting in positive work on the ocean current. This inputs a strong negative wind stress curl into the eddy, enhancing negative EPV and deepening D_E, so the downwelling within the AE1 is obvious and contributing to its increased strength. In contrast, AE2, positions directly below the typhoon's track, experiences shorter forcing duration and weakens due to the strong positive wind stress curl at the typhoon's center and shallower D_E. Furthermore, the absolute value of EPV increases in both warm eddies during the typhoon's passage, but with differing impacts. The positive EPV contributes to surface water cooling and the influx of cooler subsurface water, while the negative EPV facilitates downwelling and intensifies the influence of the warm eddies.

While numerous prior studies exploring the interaction between TCs and eddies have predominantly drawn generalized conclusions, such as the weakening (strengthening) effect of cold (warm) eddies. Conversely, TCs are recognized for strengthening cold eddies and weakening warm eddies. However, our study takes a different approach. We aim to illustrate that even when TCs encounter eddies of the same polarity, the response of these eddies to TCs exhibits variations. This nuanced response is intricately linked to factors including the relative position of the eddies and the TCs, the eddies' intensity, and the background current. It is discussed first time in the South China Sea. By analyzing wind stress curl distribution, EPV, buoyancy frequency and the relative position between the eddies and the typhoon's track, this case study provides a more nuanced understanding of the mechanisms driving these different eddy-typhoon interactions in the Northern South China Sea. Moreover, it will further improve the accuracy of TC forecasts and enhancing the simulation capabilities of air-sea coupled models.

*Data av*ailability. The six-hourly best-track typhoon datasets were accessed on 3 February 2021 by JTWC, http://www.usno.navy.mil/JTWC, JMA, https://www.jma.go.jp/jma/jma-eng/jma-center/rsmc-hp-pub-eg/besttrack.html and CMA, http://tcdata.typhoon.gov.cn. The AVISO product was accessed on 14 February 2021 by https://marine.copernicus.eu/. The AVHRR SST data was accessed on 16 March, 2022 by ftp://podaac.jpl.nasa.gov/documents/dataset_docs/avhrr_pathfinder_sst.html. The Argo data was accessed on 4 April, 2022 by https://dataselection.euro-argo.eu/. The wind data was accessed on 5 January, 2023 by

https://apps.ecmwf.int/datasets/data/interim-full-daily/levtype=sfc/. The GLORYS12V1 was accessed on 23 March, 2022 by https://marine.copernicus.eu/.

Author contributions. XYL and HZ contributed to the study conception and design. Material preparation, data collection and analysis were performed by YHH and XYL. GQH and YL contributed to the methodology. The original manuscript was prepared by XYL and YHH. All the authors contributed to the review and editing of the manuscript.

Competing interests. The contact author has declared that none of the authors has any competing interests.

Acknowledgements. These data were collected and made freely available by JTWC, JMA, CMA, AVISO, AVHRR, Argo, ECMWF, COPERNICUS. All figures were created using MATLAB, in particular using the M_Map toolbox (Pawlowicz, 2020). The authors thank the anonymous reviewers, whose feedback led to substantial improvement of the resulting analyses, figures and manuscript

Financial support. This research has been supported by the National Natural Science Foundation of China (42227901), Southern Marine Science and Engineering Guangdong Laboratory (Zhuhai), grant number SML2020SP007 and SML2021SP207; the Innovation Group Project of Southern Marine Science and Engineering Guangdong Laboratory (Zhuhai), grant number 311020004 and 311022001; the National Natural Science Foundation of China, grant number 42206005; the open fund of State Key Laboratory of Satellite Ocean Environment Dynamics, Second Institute of Oceanography, MNR, grant number QNHX2309; General scientific research project of Zhejiang Provincial Department of Education, grant number Y202250609; the Open Foundation from Marine Sciences in the First-Class Subjects of Zhejiang, grant number OFMS006; State Key Laboratory of Tropical Oceanography (South China Sea Institute of Oceanology Chinese Academy of Sciences), grant number LTO2220.

References

Cabanes, C., Grouazel, A., von Schuckmann, K., Hamon, M., Turpin, V., Coatanoan, C., Guinehut, S., Boone, C., Ferry, N., and Reverdin, G.: The CORA dataset: validation and diagnostics of ocean temperature and salinity in situ measurements, Ocean Sci. Discuss., 9, 1273-1312, 2012.

Chen, G., Hou, Y., and Chu, X.: Mesoscale eddies in the South China Sea: Mean properties, spatiotemporal variability, and impact on thermohaline structure, J. Geophys. Res.: Oceans, 116,https://doi.org/10.1029/2010jc006716, 2011.

Chen Z, Yu F, Chen Z, et al. Downward Propagation and Trapping of Near-Inertial Waves by a Westward-moving Anticyclonic Eddy in the Subtropical Northwestern Pacific Ocean[J]. Journal of Physical Oceanography, 2023.

de Boyer Montégut, C.: Mixed layer depth over the global ocean: An examination of profile data and a profile-based climatology, J. Geophys. Res.: Oceans, 109,https://doi.org/10.1029/2004jc002378, 2004.

Ezraty, R., Girard-Ardhuin, F., Piollé, J.-F., Kaleschke, L., and Heygster, G.: Arctic and Antarctic sea ice concentration and Arctic sea ice drift estimated from Special Sensor Microwave data, Département d'Océanographie Physique et Spatiale, IFREMER, Brest, France and University of Bremen Germany, 2, 2007.

Huang, L., Cao, R., and Zhang, S.: Distribution and Oceanic Dynamic Mechism of Precipitation Induced by Typhoon Lekima, American Journal of Climate Change, 11, 133-154,https://doi.org/10.4236/ajcc.2022.112007, 2022.

Huang, X. and Wang, G.: Response of a Mesoscale Dipole Eddy to the Passage of a Tropical Cyclone: A Case Study Using Satellite Observations and Numerical Modeling, Remote Sens., 14,https://doi.org/10.3390/rs14122865, 2022.

Jaimes, B. and Shay, L. K.: Enhanced Wind-Driven Downwelling Flow in Warm Oceanic Eddy Features during the Intensification of Tropical Cyclone Isaac (2012): Observations and Theory, J. Phys. Oceanogr., 45, 1667-1689,https://doi.org/10.1175/jpo-d-14-0176.1, 2015.

Jullien, S., Menkès, C. E., Marchesiello, P., Jourdain, N. C., Lengaigne, M., Koch-Larrouy, A., Lefèvre, J., Vincent, E. M., and Faure, V.: Impact of tropical cyclones on the heat budget of the South Pacific Ocean, J. Phys. Oceanogr., 42, 1882-1906,https://doi.org/10.1175/JPO-D-11-0133.1, 2012.

Kessler, W. S.: The circulation of the eastern tropical Pacific: A review, Prog. Oceanogr., 69, 181-217,https://doi.org/10.1016/j.pocean.2006.03.009, 2006.

Li, Q., Sun, L., Liu, S., Xian, T., and Yan, Y.: A new mononuclear eddy identification method with simple splitting strategies, Remote Sens. Lett., 5, 65 - 72,https://doi.org/10.1080/2150704x.2013.872814, 2014.

Li, X., Zhang, X., Fu, D., and Liao, S.: Strengthening effect of super typhoon Rammasun (2014) on upwelling and cold eddies in the South China Sea, J. Oceanol. Limnol., 39, 403-419,https://doi.org/10.1007/s00343-020-9239-x, 2021.

Lin, I. I., Chou, M.-D., and Wu, C.-C.: The Impact of a Warm Ocean Eddy on Typhoon Morakot (2009): A Preliminary Study from Satellite Observations and Numerical Modelling, TAO: Terrestrial, Atmospheric and Oceanic Sciences, 22,https://doi.org/10.3319/tao.2011.08.19.01(tm), 2011.

Lin, I. I., Wu, C.-C., Emanuel, K. A., Lee, I. H., Wu, C.-R., and Pun, I.-F.: The Interaction of Supertyphoon Maemi (2003) with a Warm Ocean Eddy, Mon. Weather Rev., 133, 2635-2649,https://doi.org/10.1175/MWR3005.1, 2005.

Liu, F. and Tang, S.: Influence of the Interaction Between Typhoons and Oceanic Mesoscale Eddies on Phytoplankton Blooms, J. Geophys. Res.: Oceans, 123, 2785-2794,https://doi.org/10.1029/2017jc013225, 2018.

Liu, S.-S., Sun, L., Wu, Q., and Yang, Y.-J.: The responses of cyclonic and anticyclonic eddies to typhoon forcing: The vertical temperature-salinity structure changes associated with the horizontal convergence/divergence, J. Geophys. Res.: Oceans, 122, 4974-4989,https://doi.org/10.1002/2017JC012814, 2017.

Lu, Z., Wang, G., and Shang, X.: Response of a Preexisting Cyclonic Ocean Eddy to a Typhoon, J. Phys. Oceanogr., 46, 2403-2410,https://doi.org/10.1175/jpo-d-16-0040.1, 2016.

642 Lu, Z., Wang, G., and Shang, X.: Strength and Spatial Structure of the Perturbation Induced by a Tropical
643 Cyclone to the Underlying Eddies, J. Geophys. Res.: Oceans, 125,https://doi.org/10.1029/2020jc016097,
644 2020.
645 Lu, Z., Wang, G., and Shang, X.: Observable large-scale impacts of tropical cyclones on subtropical gyre,
646 J. Phys. Oceanogr.,https://doi.org/10.1175/JPO-D-22-0230.1, 2023.
647 Ma, Z., Zhang, Z., Fei, J., and Wang, H.: Imprints of Tropical Cyclones on Structural Characteristics of
648 Mesoscale   Oceanic   Eddies   Over   the   Western   North   Pacific,   Geophys.   Res.   Lett.,
649 48,https://doi.org/10.1029/2021gl092601, 2021.
650 Ma, Z., Fei, J., Liu, L., Huang, X., and Li, Y.: An Investigation of the Influences of Mesoscale Ocean
651 Eddies   on   Tropical   Cyclone   Intensities,   Mon.   Weather   Rev.,   145,   1181-
652 1201,https://doi.org/10.1175/mwr-d-16-0253.1, 2017.
653 Ning, J., Xu, Q., Zhang, H., Wang, T., and Fan, K.: Impact of Cyclonic Ocean Eddies on Upper Ocean
654 Thermodynamic Response to Typhoon Soudelor, Remote Sens., 11,https://doi.org/10.3390/rs11080938,
655 2019.
656 Oey, L. Y., Ezer, T., Wang, D. P., Fan, S. J., and Yin, X. Q.: Loop Current warming by Hurricane Wilma,
657 Geophys. Res. Lett., 33,https://doi.org/10.1029/2006gl025873, 2006.
658 Price, J. F.: Upper Ocean Response to a Hurricane, J. Phys. Oceanogr.,https://doi.org/10.1175/1520-
659 0485(1981)011%3C0153:UORTAH%3E2.0.CO;2, 1981.
660 Pujol, M.-I., Faugère, Y., Taburet, G., Dupuy, S., Pelloquin, C., Ablain, M., and Picot, N.: DUACS
661 DT2014: the new multi-mission altimeter data set reprocessed over 20 years, Ocean Sci., 12, 1067-
662 1090,https://doi.org/10.5194/os-12-1067-2016, 2016.
663 Rudzin, J. E. and Chen, S.: On the dynamics of the eradication of a warm core mesoscale eddy after the
664 passage   of   Hurricane   Irma   (2017),   Dyn.   Atmos.   Oceans,
665 100,https://doi.org/10.1016/j.dynatmoce.2022.101334, 2022.
666 Shang, X.-d., Zhu, H.-b., Chen, G.-y., Xu, C., and Yang, Q.: Research on Cold Core Eddy Change and
667 Phytoplankton Bloom Induced by Typhoons: Case Studies in the South China Sea, Adv. Meteorol., 2015,
668 1-19,https://doi.org/10.1155/2015/340432, 2015.
669 Shay, L. K. and Jaimes, B.: Mixed Layer Cooling in Mesoscale Oceanic Eddies during Hurricanes
670 Katrina and Rita, Mon. Weather Rev., 137, 4188-4207,https://doi.org/10.1175/2009mwr2849.1, 2009.
671 Shay, L. K. and Jaimes, B.: Near-Inertial Wave Wake of Hurricanes Katrina and Rita over Mesoscale
672 Oceanic Eddies, J. Phys. Oceanogr., 40, 1320-1337,https://doi.org/10.1175/2010jpo4309.1, 2010.
673 Shay, L. K., Goni, G. J., and Black, P. G.: Effects of a Warm Oceanic Feature on Hurricane Opal, Mon.
674 Weather   Rev.,   128,   1366-1383,https://doi.org/10.1175/1520-
675 0493(2000)128<1366:EOAWOF>2.0.CO;2, 2000.
676 Song, D., Guo, L., Duan, Z., and Xiang, L.: Impact of Major Typhoons in 2016 on Sea Surface Features
677 in the Northwestern Pacific, Water, 10,https://doi.org/10.3390/w10101326, 2018.
678 Sun, J., Ju, X., Zheng, Q., Wang, G., Li, L., and Xiong, X.: Numerical Study of the Response of Typhoon
679 Hato (2017) to Grouped Mesoscale Eddies in the Northern South China Sea, J. Geophys. Res.: Atmos.,
680 128,https://doi.org/10.1029/2022jd037266, 2023.
681 Sun, L., Yang, Y., Xian, T., Lu, Z., and Fu, Y.: Strong enhancement of chlorophyll a concentration by a
682 weak typhoon, Mar. Ecol. Prog. Ser., 404, 39-50,https://doi.org/10.3354/meps08477, 2010.
683 Sun, L., Li, Y.-X., Yang, Y.-J., Wu, Q., Chen, X.-T., Li, Q.-Y., Li, Y.-B., and Xian, T.: Effects of super
684 typhoons on cyclonic ocean eddies in the western North Pacific: A satellite data-based evaluation

between 2000 and 2008, J. Geophys. Res.: Oceans, 119, 5585-5598,https://doi.org/10.1002/2013jc009575, 2014.

Thompson, B. and Tkalich, P.: Mixed layer thermodynamics of the Southern South China Sea, Clim. Dyn., 43, 2061-2075,https://doi.org/10.1007/s00382-013-2030-3, 2014.

Wada, A. and Usui, N.: Impacts of Oceanic Preexisting Conditions on Predictions of Typhoon Hai-Tang in 2005, Adv. Meteorol., 2010, 756071,https://doi.org/10.1155/2010/756071, 2010.

Walker, N. D., Leben, R. R., and Balasubramanian, S.: Hurricane-forced upwelling and chlorophyllaenhancement within cold-core cyclones in the Gulf of Mexico, Geophys. Res. Lett., 32, n/a-n/a,https://doi.org/10.1029/2005gl023716, 2005.

Wang, G., Su, J., Ding, Y., and Chen, D.: Tropical cyclone genesis over the south China sea, J. Mar. Syst., 68, 318-326,https://doi.org/10.1016/j.jmarsys.2006.12.002, 2007.

Wang, G., Zhao, B., Qiao, F., and Zhao, C.: Rapid intensification of Super Typhoon Haiyan: the important role of a warm-core ocean eddy, Ocean Dyn., 68, 1649-1661,https://doi.org/10.1007/s10236-018-1217-x, 2018.

Xiu, P., Chai, F., Shi, L., Xue, H., and Chao, Y.: A census of eddy activities in the South China Sea during 1993–2007, J. Geophys. Res.: Oceans, 115,https://doi.org/10.1029/2009jc005657, 2010.

Yan, Y., Li, L., and Wang, C.: The effects of oceanic barrier layer on the upper ocean response to tropical cyclones, J. Geophys. Res.: Oceans, 122, 4829-4844,https://doi.org/10.1002/2017jc012694, 2017.

Yu, F., Yang, Q., Chen, G., and Li, Q.: The response of cyclonic eddies to typhoons based on satellite remote sensing data for 2001–2014 from the South China Sea, Oceanologia, 61, 265-275,https://doi.org/10.1016/j.oceano.2018.11.005, 2019.

Yu, J., Lin, S., Jiang, Y., and Wang, Y.: Modulation of Typhoon-Induced Sea Surface Cooling by Preexisting Eddies in the South China Sea, Water, 13,https://doi.org/10.3390/w13050653, 2021.

Zhang, H.: Modulation of Upper Ocean Vertical Temperature Structure and Heat Content by a Fast-Moving Tropical Cyclone, J. Phys. Oceanogr., 53, 493-508,https://doi.org/10.1175/jpo-d-22-0132.1, 2022.

Zhang, H., Chen, D., Zhou, L., Liu, X., Ding, T., and Zhou, B.: Upper ocean response to typhoon Kalmaegi (2014), J. Geophys. Res.: Oceans, 121, 6520-6535,https://doi.org/10.1002/2016jc012064, 2016.

Zhang, Y., Zhang, Z., Chen, D., Qiu, B., and Wang, W.: Strengthening of the Kuroshio current by intensifying tropical cyclones, Science, 368, 988-993,https://doi.org/10.1126/science.aax5758, 2020.